# Journal of Materials Chemistry A

Accepted Manuscript

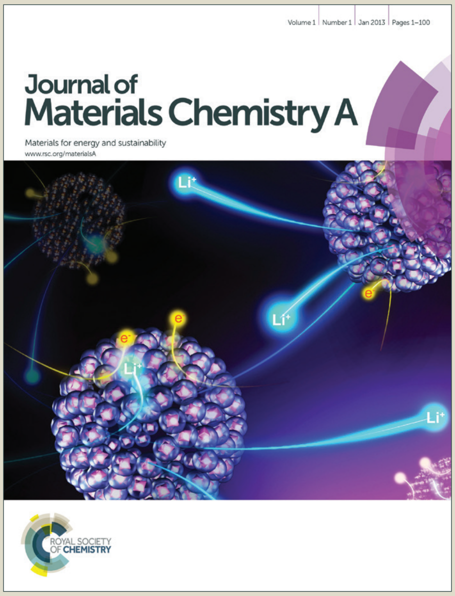

ROYAL SOCIETY OF CHEMISTRY

www.rsc.org/materialsA

# Graphical Abstract

## Graphic

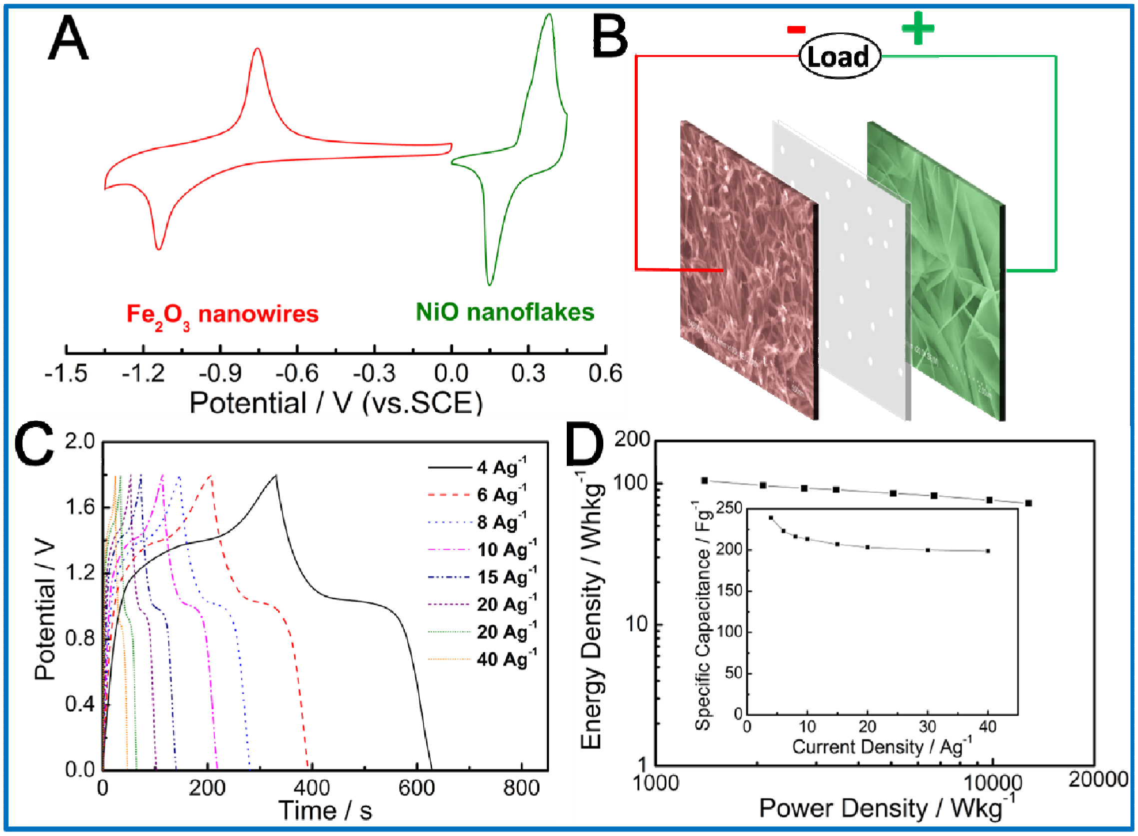

## Text

A novel low-cost anode of homogenous $Fe_2O_3$ nanowires on CFP was developed, achieving a high specific capacitance in 0~-1.35 V. Matching it with NiO nanoflakes cathode, an extremely high energy density of 105 Wh kg$^{-1}$ is obtained at 1400 W kg$^{-1}$ and still retains 72.6 Wh kg$^{-1}$ at 12700 W kg$^{-1}$ for the AASCs, which is much superior to previously reported AASCs and exceeding those of Ni-MH batteries.

Journal of
Materials Chemistry A

Cite this: DOI: 10.1039/c0xx00000x

www.rsc.org/xxxxxx

**ARTICLE TYPE**

# The Perfect Matching between Low-cost $Fe_2O_3$ Nanowires Anode and NiO Nanoflakes Cathode Significantly Enhances the Energy Density of Asymmetric Supercapacitors

**Qianqiu Tang,[a] Wenqiang Wang,[a] and Gengchao Wang*[a]**

***Received (in XXX, XXX) Xth XXXXXXXXX 20XX, Accepted Xth XXXXXXXXX 20XX***
**DOI: 10.1039/b000000x**

The real-world application of supercapacitors is hindered by their relatively low energy density compared with rechargeable batteries. Even with tremendous efforts in developing cathodes for aqueous asymmetric supercapacitors (AASCs), their supercapacitive performance is still severely restricted by the low specific capacitance of anodes which mostly consist of carbonaceous materials. We developed a novel low-cost anode of homogenous $Fe_2O_3$ nanowires growing on carbon fiber paper (CFP), achieving a high specific capacitance of 908 F $g^{-1}$ at 2A $g^{-1}$ and excellent rate performance (90 % capacitance retention up to 10 A $g^{-1}$) in a wide negative potential window of 0~-1.35 V. Such an excellent supercapacitive performance makes it a perfect anode compared with other reported ones. Matching it with NiO nanoflakes cathode (1520 F $g^{-1}$ at 2 A $g^{-1}$ in 0~0.45 V) on CFP, an extremely high energy density of 105 Wh $kg^{-1}$ is obtained at the power density of 1400 W $kg^{-1}$ and still retains 72.6 Wh $kg^{-1}$ at 12700 W $kg^{-1}$ for the AASCs, which is much superior to previously reported AASCs and even exceeding those of Ni-MH batteries.

## 1. Introduction

With the increasing demand for energy storage technologies, supercapacitors have attracted enormous research attention due to their high power density and long cycle life compared with rechargeable batteries. However, their energy densities are still far lagging behind, which severely restricts their practical application. According to the equation of $E=1/2CU^2$, the energy density (E) is more dominated by the operating potential window (U). Although the organic electrolyte exhibits a higher potential window of up to 3 V than aqueous ones of 1.2 V, aqueous-based supercapacitors exhibit higher electronic conductivity, electrochemical safety and easier manufacturing. Besides, by assembling aqueous-based asymmetric supercapacitors (AASCs) with different cathodes and anodes, the operating potential window can be enhanced to 1.6~2.0 V. Thus, AASCs show great promise for high energy density applications.[1-3]

Another approach to improve the energy density is to utilize nanostructured pseudocapacitive electrode materials based on reversible redox reactions, whose energy density usually exceeds that of carbon materials involving double layer charge storage. Besides, nanostructurization provides more accessible surface area for energy storage and facilitates electrolyte penetration.[4] Fig. 1A[5-21] summarizes the working potential windows of various pseudocapacitive materials in aqueous electrolyte. Even though tremendous research efforts have been devoted to the nanostructurization of cathode materials with average potential window above 0 V, there are only a few reports of nanostructured pseudocapacitive anode materials. At present, carbonaceous materials are still the most widely used anodes, such as activated carbon[22], graphene[23, 24] and nitrogen-doped carbons[25]. However, from Fig. 1B[7, 22-32], carbonaceous materials exhibits quite small specific capacitances of 100~250 F $g^{-1}$ compared with pseudocapacitive cathodes of up to 600~2500 F $g^{-1}$. As to the few reported pseudocapacitive anodes, their electrochemical performance is far from satisfactory such as low specific capacitance[26, 27, 33]and poor cycling stability[20]. Thus, higher mass is needed for anodes so as to meet the charge balance with the cathodes, having a negative impact on the overall specific capacitance and the energy density of the assembled AASCs. Thus, it is critical to improve the capacitive behavior of the pseudocapacitive anodes by nanostructurization in order to match with cathodes.

Among the few reported pseudocapacitive anodes, $Fe_2O_3$ exhibits significant advantageous such as low cost, environmental friendliness and safety[20, 34-37] compared with toxic and expensive $V_2O_5$[17, 38] and $MoO_3$[33, 39, 40]. However, the intrinsic poor conductivity and aggregated morphology of $Fe_2O_3$-based electrodes restricts the utilization of their electrochemical active sites, hindering the improvement of their specific capacitances. An emerging new concept is to grow electroactive nanostructures on conductive substrates to be directly used as binder-free electrodes for supercapacitors. Since every electroactive nanostructure is directly attached to the conductive substrate, the poor conductivity of the electroactive material is no longer a big concern. And the nanostructured morphology facilitates the penetration of electrolyte to the inner part of electrodes, enhancing the utilization of their pseudocapacitance. Furthermore, the preparation process of electrodes is significantly simplified by avoiding the use of conductive agents and binders.[41] However, as far as we know, there are no reports of nanostructured $Fe_2O_3$ anodes directly growing on conductive substrates used in AASCs.

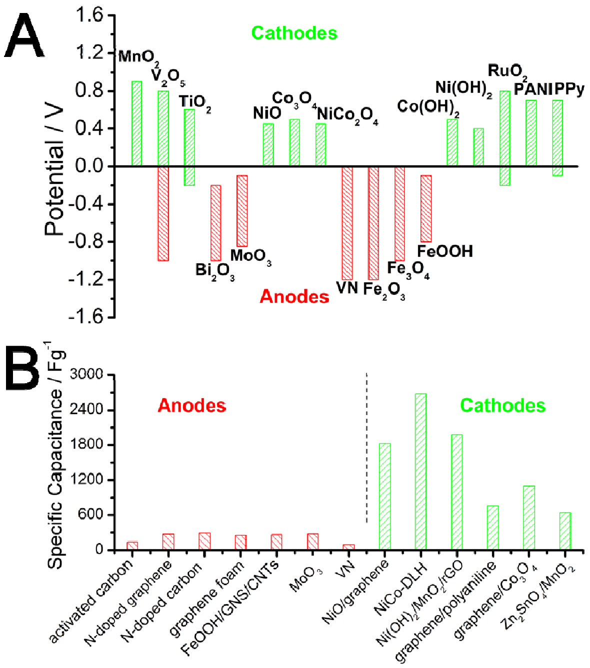

**Fig. 1.** (A) The working potential window of various pseudocapacitive electrode materials in aqueous electrolyte. (B) Specific capacitance of selected anode and cathode materials.

In this paper, we developed a modified hydrothermal process followed by calcination to prepare a novel low-cost anode of homogenous $Fe_2O_3$ nanowires on carbon fiber paper (CFP). By decreasing the hydrothermal temperature, we successfully obtained $Fe_2O_3$ nanowires on CFP with a diameter of only about 10 nm, which is much smaller than previous reports. Due to the favorable nanostructure, it exhibits an improved specific capacitance of 908 F $g^{-1}$ at 2 A $g^{-1}$ in a wide potential window of 0~-1.35 V, making it a perfect anode candidate to match with of NiO nanoflakes cathode (1520 F $g^{-1}$ at 2 A $g^{-1}$). By enhancing the supercapacitive performance of $Fe_2O_3$ nanowires anode compared with previous carbonaceous anodes or other metal-oxide based ones, a maximum high energy density of 105 Wh $kg^{-1}$ is obtained at the power density of 1400 W $kg^{-1}$ for the NiO nanoflakes//$Fe_2O_3$ nanowires AASCs. Such an excellent energy performance of AASCs is superior to previously reported AASCs and even exceeding those of Ni-MH batteries.

## 2. Experimental

### 2.1 Growth of $Fe_2O_3$ nanowires on carbon fiber paper (CFP).

We adopted a modified method from previous reports[35, 41] and achieved a more favorable condition for the nanostructurization of $Fe_2O_3$. Prior to deposition, the carbon fiber paper (Toray Composites Inc., Japan) was cut into pieces of 1.5 cm×1.5 cm, and then treated with 3:1 $H_2SO_4/HNO_3$ mixed acid at 60 °C for 2 h. For the hydrothermal deposition of $Fe_2O_3$ nanowires, 6.0 mmol $FeCl_3\cdot 6H_2O$, 7.5 mmol $Na_2SO_4$ were homogeneously dispersed in 300 mL deionized water. Then 40 mL as-prepared mixed solution and the treated CFP were transferred to a 50 mL Teflon lined stainless autoclave, which was then sealed and maintained at 60 °C for 12 h. After the autoclave was cooled to room temperature, the carbon fiber paper pieces with grown precursor were taken out and then ultrasonically treated for 20 min to remove the adsorbed deposition. Finally, they were calcinated at 400 °C for 2h under the Ar atmosphere with the heating rate of 1 °C $min^{-1}$. In comparison, $Fe_2O_3$ bundles were also grown on CFP under a higher hydrothermal condition of 90 °C for 12h with no other conditions changed.

### 2.2 Growth of NiO nanoflakes on carbon fiber paper (CFP).

For the deposition of NiO nanoflakes, we use a similar process as previous reports.[42] Mixed acid treatment was also adopted on CFP before deposition. 30 mmol $Ni(NO_3)_2\cdot 6H_2O$, 240 mmol $CO(NH_2)_2$ and 30 mmol $NH_4F$ were dispersed in 300 mL deionized water. Then 40 mL as-prepared mixed solution and the treated CFP were transferred to a 50 mL Teflon lined stainless autoclave, which was then sealed and maintained at 100 °C for 5 h. And the post calcination process was carried out at 400 °C for 4 h under the Ar atmosphere, with the heating rate of 1 °C $min^{-1}$.

### 2.3 Characterization

The morphologies of the as-prepared samples were observed by field-emission scanning electron microscope (FE-SEM, Hitachi S-4800) and high resolution transmission electron microscopy (HRTEM, JEOL JEM-2100). Powder X-ray diffraction (XRD) patterns were performed in a Rigaku D/Max 2550 VB/PC X-ray diffractometer using Cu (Kα) radiation with the 2θ-angle recorded from 5~75°. X-ray photoelectron spectroscopy (XPS) was recorded with a thermo scientific ESCALAB 250Xi X-ray photoelectron spectrometer equipped with a monochromatic Al Kα X-ray source (1486.6 eV).

### 2.4 Electrochemical measurements

For the three-electrode mode measurements, the $Fe_2O_3$ nanowires anodes and NiO nanoflakes cathodes were directly used as the working electrodes, a saturated calomel electrode (SCE) was used as reference electrode and a Pt sheet as counter electrode. For the fabrication of AASCs, the $Fe_2O_3$ nanowires anode and NiO nanoflakes cathode were sandwiched with a modified hydrophilic polypropylene separator [PPAT-CN1(2), Shanghai Shilong Hi-Tech Corp., Ltd]. The electrolyte was 2M KOH aqueous solution.The active material mass ratio of $Fe_2O_3$/NiO of 1/ 1.8 was calculated based on the charge balance between the cathodes and anodes of $q^+ = q^-$, where $q = C_s \varDelta Vm$, $C_s$: the specific capacitance, $\varDelta V$: the potential window, and m: the mass of the electrode. The cyclic voltammetry, galvanostatic charge-discharge and electrochemical impedance spectroscopy (EIS) measurements were performed on a CHI 660D electrochemical workstation. And the cycling stability was performed by galvanostatic charge/discharge test with a program testing system (LAND CT2001A) using cell supercapacitors. Besides, for the NiO nanoflakes cathodes, they were activated by repeated CV at 20 mV $s^{-1}$ for 500 cycles until the CV curves in the potential window of -0.4~0.5 V began to collapse with each other before all the electrochemical measurements.

The specific capacitance of the single electrode material ($Cs$) was calculated according to a three-electrode data with the following equation: $Cs = C/m = I\Delta t/m\Delta V$, where $I$ is the discharge current, $m$ is the mass of active electrode material, $\Delta t$ is the discharging time and $\Delta V$ is the voltage change during the discharging time after IR drop. The specific capacitance of the total AASCs device ($C_t$) was calculated by the two-electrode datas following a similar equation of $C_t = C_t/m_t = I\Delta t/m_t\Delta V$, where $I$ is the discharge current, $m_t$ is the total mass of active anode and cathodes materials, $\Delta t$ is the discharging time and $\Delta V_t$ is the voltage change during the discharging time after IR drop. The energy density ($E$, W h kg$^{-1}$) and the power density ($P$, W kg$^{-1}$) for a supercapacitor cell can be estimated using the following equations: $E = 0.5\ C_TV^2/3.6$ and $P = E\times3600\ /\ t$, where $C_T$ (F g$^{-1}$) is the total specific capacitance of the supercapacitor cell, $V$ (V) is the voltage range after IR drop, and $t$ (s) is the discharge time.

## 3. Results and discussion

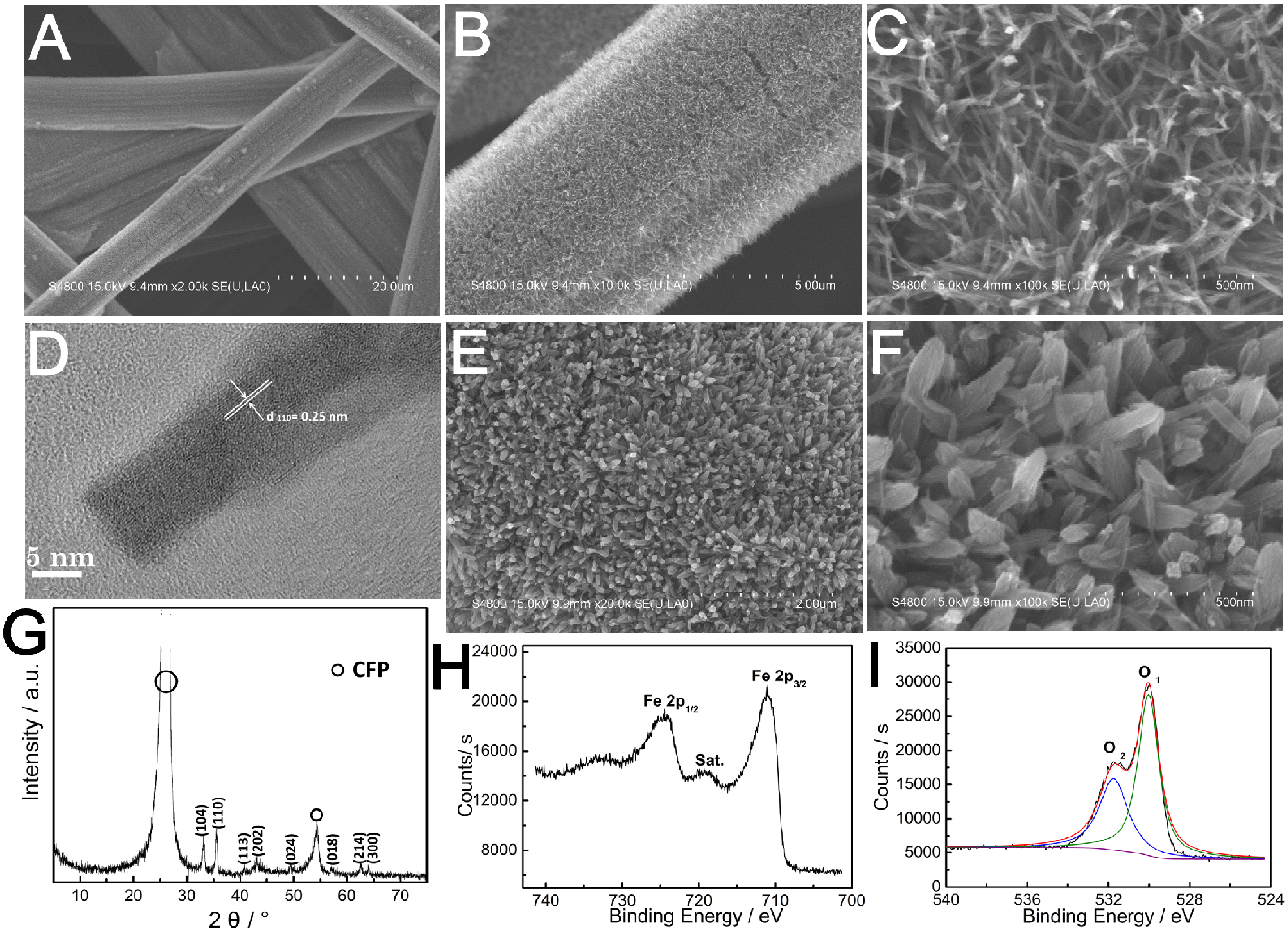

**Fig. 2**. (A~C) FE-SEM images of $Fe_2O_3$ nanowires on CFP. (D) High-magnification HRTEM images of $Fe_2O_3$ nanowires scratched down from the CFP substrate (inserted with corresponding low-magnification HRTEM image). (E, F) FE-SEM images of $Fe_2O_3$ bundles on CFP. (G) XRD pattern of $Fe_2O_3$ nanowires on CFP. (H) Fe2p and (I) O1s XPS spectrum of $Fe_2O_3$ nanowires on CFP.

Herein, carbon fiber paper (CFP) is chosen as the conductive substrate for the growth of electrochemical active materials due to its high conductivity and loosely packed fiber structure, which is more favorable for electrolyte penetration to the electrodes. For the growth of $Fe_2O_3$ anodes, $Na_2SO_4$ was employed as a structure-directing agent to facilitate the relatively uniform growth of 1D nanowires.[43] From Fig. 2A and 2B, the homogenous distribution of $Fe_2O_3$ nanowires is quite obvious. Here, the homogeneous and heterogeneous nucleation phenomena need to be taken into consideration so as to explain for the ability to grow into nanowires on a substrate.[44] In most cases, homogeneous nucleation of solid phases (metal oxide in particular) requires a higher activation energy barrier and therefore heteronucleation will be promoted and energetically more favorable. Thus nucleation may take place at a lower saturation ratio onto CFP substrate than in solution. Besides, from the high-magnification image shown in Fig. 2C, it can be seen that the $Fe_2O_3$ nanowires with the average diameter of about 10 nm are grown almost perpendicular to the substrate rather than along the CFP surface. It is due to the fact that epitaxial crystal growth will take place from the heterogeneous nuclei along the easy direction of crystallization when the nuclei rate is limited by the precipitation conditions, while high concentration of precursor (as the condition in our synthesis) generate the perpendicular crystalline growth to the substrate.

In order to provide insights into the micromorphology of the $Fe_2O_3$ nanowires, we scratched them down from the CFP substrate. From the HRTEM image shown in Fig. 2D, it confirms the small diameter of $Fe_2O_3$ nanowires to be about 10 nm. Besides, the lattice fringes with a spacing of 0.25 nm is in good agreement with the spacing of the (110) plane of $Fe_2O_3$. In comparison, when increasing the hydrothermal temperature from 60 to 90 °C with no other preparation condition changed, it is found that the $Fe_2O_3$ bundles (shown in Fig. 2E and 2F) exhibit a much larger diameter of 50~100 nm. It is due to the fact that grown precursor obtained through hydrothermal process were more easily agglomerated into bundles under higher temperatures, probably owing to the high surface energy resulting from the small size of nanowires. Furthermore, our modified synthesis shows some advantages over previous literatures[36, 43] with the diameter of $Fe_2O_3$ nanowires to be 35~50 nm. Thus, the optimized preparation condition plays a significant role in determining the nanostructures of the as-grown $Fe_2O_3$ nanowires, which is also critical to the electrochemical performance of electrodes to be discussed later.

Furthermore, the XRD pattern (Fig. 2G) of $Fe_2O_3$ nanowires on CFP exhibits all the peaks which can be well assigned to $\alpha$-$Fe_2O_3$ (JCPDS no. 33-0664). We also performed the X-ray photoelectron spectroscopy (XPS) measurements to study the oxidation state of the $Fe_2O_3$ nanowires. Fig. 2H shows the Fe $2p_{3/2}$ and Fe $2p_{1/2}$ peaks centered at 711.0 and 724.5 eV, which are typical of $Fe^{3+}$ of $Fe_2O_3$ and much higher than the 709 and 722.6eV corresponding to $Fe^{2+}$.[45] And at 718.8 eV, a satellite peak associated with Fe $2p_{3/2}$ appears, which does not overlap either with Fe $2p_{3/2}$ or Fe $2p_{3/2}$ peaks. This satellite peak located approximately 8 eV higher than the main Fe $2p_{3/2}$ further confirms the $Fe^{3+}$ species.[45] As to the O 1s spectra (Fig. 2I), two peaks (denoted as $O_1$ and $O_2$) can be clearly identified. The $O_1$ peak centered at about 530.0 eV is attributed to the lattice oxygen as Fe-O-Fe, and the $O_2$ peak at 531.8 eV correspond to Fe-O-H, showing that the surface of $Fe_2O_3$ nanowires is hydrolyzed to some extent.[46, 47]

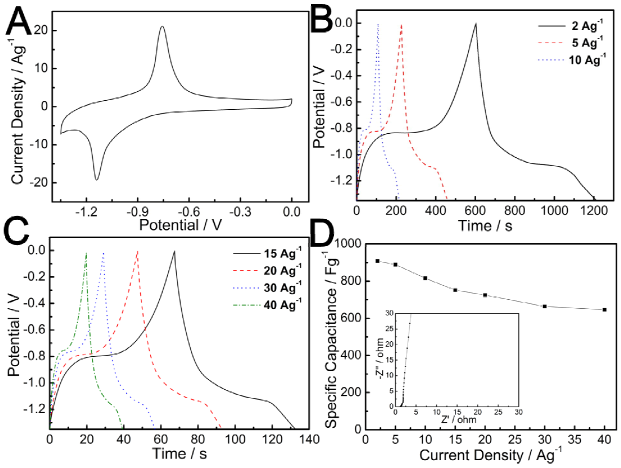

**Fig. 3**. Electrochemical performance of $Fe_2O_3$ nanowires anode growing on CFP with three-electrode measurement in 2 M KOH (A) Cyclic voltammetry curve at 5 mV $s^{-1}$. (B, C) Galvanostatic charge-discharge curves at various current densities from 2 to 40 A $g^{-1}$. (D) Specific capacitances at various current densities (inserted with Nyquist plot in the frequency from 100 kHz to 0.01Hz).

To evaluate the electrochemical performance of $Fe_2O_3$ nanowires cathode, we obtained the cyclic voltammetry (CV) curve at 5 mV $s^{-1}$ using the three-electrode measurement (Fig. 3A). A pair of well-defined peaks at about -0.75 V for the anodic scan and about -1.15 V for the cathodic scan can be clearly observed, which are ascribed to the reversible oxidation and reduction process between $Fe^{3+}$ and $Fe^{2+}$ following the reaction of $Fe^{III}{}_2O_3+2e^- +3H_2O \leftrightarrow 2Fe^{II}(OH)_2 +2OH^-$. Correspondingly, the galvanostatic charge-discharge (GCD) curves (Fig. 3B and 3C) at various current densities exhibit obvious platforms of about -0.8 V and -1.15 V, respectively. Besides, from the CV and GCD curves, no obvious hydrogen evolution is observed, which is due to the high hydrogen evolution overpotential of the $Fe_2O_3$ nanowires growing on the CFP. Thus, it can be conclude that the potential of 0~-1.35 V is a safe potential window for the as-grown $Fe_2O_3$ nanowires, and such broad potential window is beneficial to enhancing the energy density of fabricated two-electrode asymmetric supercapacitors. Furthermore, calculated from the GCD curves, specific capacitances are obtained (Fig. 3D). At the current density of 2 A $g^{-1}$, the as-grown $Fe_2O_3$ nanowires exhibit a high specific capacitance of 908 F $g^{-1}$. Even at a high current density of 10 and 40 A $g^{-1}$, it still retains a specific capacitance of 816 and 646 F $g^{-1}$, respectively, showing an excellent rate performance. The inserted Nyquist plot shows a quite a small real axis intersection point of 1.1 Ω and a negligible semicircle in the high frequency region, showing their small ohmic resistance and quite a low charge-transfer resistance. In comparison, the $Fe_2O_3$ bundles obtained at a higher hydrothermal temperature of 90 °C exhibit a relatively poorer electrochemical performance (shown in Fig. S1). A lower specific capacitance of 693 $Fg^{-1}$ is obtained at 2 A $g^{-1}$, and it rapid decrease to only 367 $Fg^{-1}$ at 40 $Ag^{-1}$, showing a worse rate performance. The excellent electrochemical performance of the as-grown $Fe_2O_3$ nanowires can be safely ascribed to their quite homogeneous nanostructures with a small diameter of only about 10 nm. It facilitates the electrolyte flow to more accessible electrochemical active sites of $Fe_2O_3$ nanowires, enhancing the capacitive performance as a result.

As far as we know, the electrochemical performance of the as-grown $Fe_2O_3$ nanowires in the wide negative potential window is by far the most excellent among the reported anodes of supercapacitors. For example, for carbon-based electrodes including template carbons and doped graphene, the highest reported specific capacitance is that of highly functionalized activated carbons with colossal pseudocapacitance, which is about 550 F $g^{-1}$ at 0.25 A $g^{-1}$ and about 350 F $g^{-1}$ at 10 A $g^{-1}$.[48] As to the metal-oxide anodes, graphene/$Fe_2O_3$[20] exhibits a specific capacitance of 908 F $g^{-1}$ at 2 A $g^{-1}$ and about 640 F $g^{-1}$ at 40 A $g^{-1}$, which are comparable to our as-grown $Fe_2O_3$ nanowires. However, it should be noticed that the high specific capacitance value of $Fe_2O_3$ nanowires is obtained in a relatively higher potential window of 0~-1.35 V. Thus, we can safely draw the conclusion that compared with other reported anodes, the as-grown $Fe_2O_3$ nanowires electrode is a perfect anode with their high specific capacitance.

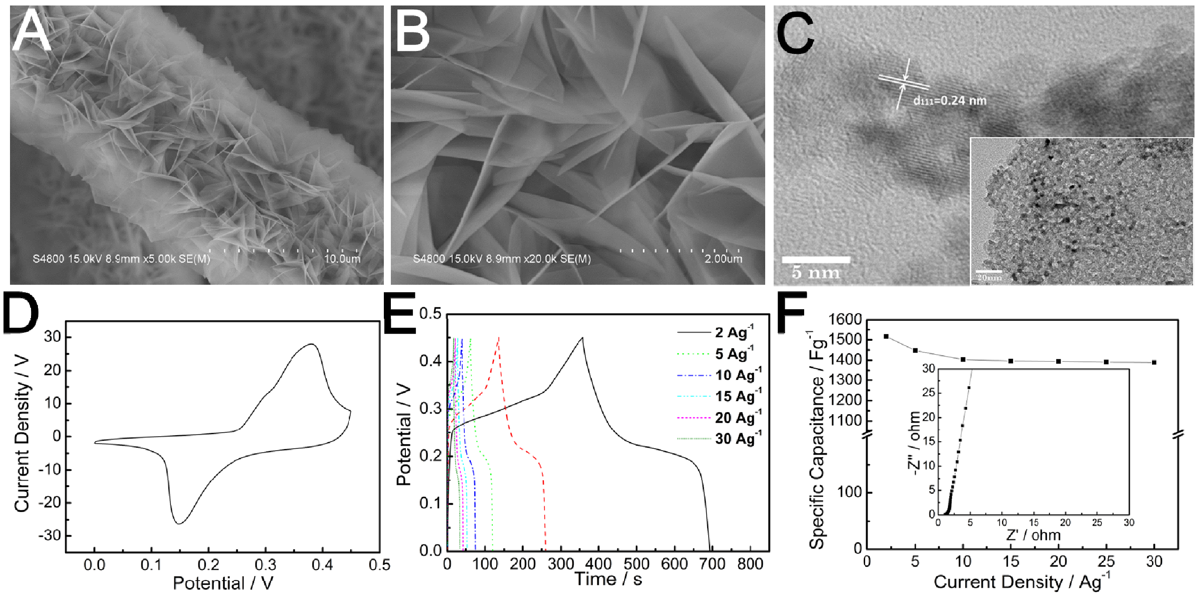

**Fig. 4**. (A) Low- and (B) high-magnification FE-SEM images of NiO nanoflakes on CFP. (C) High-magnification HRTEM images of NiO nanoflakes scratched down from the CFP substrate (inserted with corresponding low-magnification HRTEM image). Electrochemical performance of NiO nanoflakes cathode growing on CFP with three-electrode measurement in 2 M KOH (D) cyclic voltammetry curve at 5 $mVs^{-1}$. (E) galvanostatic charge-discharge curves at various current densities from 2 to 30 $Ag^{-1}$. (F) Specific capacitances at various current densities (inserted with Nyquist plot in the frequency from 100 kHz to 0.01Hz).

As to the cathodes, NiO is grown on CFP through a similar process as that in previous reports[42]. As shown in Fig. 4A and 4B, we can see that NiO nanoflakes are homogeneously grown on CFP. And the HRTEM image inserted in Fig. 4C shows that the NiO nanoflakes are composed of numerous nanoparticles and nanopores. Well-resolved lattice spacings observed from HRTEM images (Fig. 4C) corresponded to a d-spacing value of 0.24 nm, consistent with the (111) planes of a cubic-phase NiO. Furthermore, the XRD pattern (Fig. S2A) also confirmed the formation of NiO with cubic crystal structure (JCPDS card No. 47-1049). XPS measurement (Fig. S2B and S2C) is conducted to investigate the valence state of Ni element in NiO. The main $2P_{3/2}$ spectrum at 854.9 eV is standard for $Ni^{2+}$. And there are also two satellite peaks of nickel at the high binding energy side of the Ni $2p_{3/2}$ and $2p_{1/2}$ edge.[49, 50]

Accordingly, we study the electrochemical performance of NiO nanoflakes cathode with three-electrode measurement in the positive potential window of 0~0.45 V. Before the measurement, the as-grown NiO nanoflakes on CFP is electrochemical activated by CV at the scan rate of 20 mV $s^{-1}$ for 500 cycles, which is like the process of activating $NiCo_2O_4$ nanowires in our previous report.[23] From Fig. 4D, two sharp peaks are observed in the CV curve, which reflect the reversible redox reaction of $Ni^{II}O + OH^- \leftrightarrow Ni^{III}OOH + e^-$. The GCD curves shown in Fig. 4E shows obvious charge and discharge platforms, which are in good agreement with the redox peaks in CV curves. Furthermore, the as-grown NiO nanoflakes exhibit a large specific capacitance of 1520 F $g^{-1}$ at 2 A $g^{-1}$ and 91.6% capacitance retention rate at a high current density of 30 A $g^{-1}$ (shown in Fig. 4F). The small ohmic resistance (real axis intersection point) and charge-transfer resistance (the diameter of the semicircle) can fully explain their excellent rate performance.

Considering the excellent electrochemical performance of both the $Fe_2O_3$ nanowires anode and NiO nanoflakes cathode, we can see that CFP is an ideal conductive substrate for the hydrothermal growth of electrochemical active materials followed by calcination. Without redundant surfactant or template, homogeneous nanostructures are grown on the CFP substrate with strong cohesion initiated by heteronucleation. The unique nanostructure is quite beneficial to the rapid electrolyte flow to more accessible electrochemical active sites, and thus $Fe_2O_3$ nanowires anode and NiO nanoflakes cathode can fully utilize their large theoretical pseudocapacitance in the corresponding complementary potential windows.

Based upon above experimental results and discussion, the perfect matching between NiO nanowires and $Fe_2O_3$ nanoflakes on CFP is quite obvious. From Fig. 5A, they exhibit large pseudocapacitance in the exactly complementary potential windows. Thus, the NiO nanowires and $Fe_2O_3$ nanoflakes on CFP were used as cathodes and anodes to assemble NiO nanowires//$Fe_2O_3$ nanoflakes AASCs, respectively (as shown in Fig. 5B). The energy storage mechanism based upon faradaic reactions is explained as follows. During charging of the as-assembled AASCs, the anode of $Fe_2O_3$ nanowires undergo reduction process as $1/2\ Fe^{III}{}_2O_3+e^- +3/2H_2O \rightarrow Fe^{II}(OH)_2 +OH^-$ at the potential of about -1.15 V, and the cathode of NiO nanoflakes are oxidized following the process of $Ni^{II}O + OH^- \rightarrow Ni^{III}OOH + e^-$ at about 0.35 V. As to discharging, the process reverses. This explains why the NiO nanowires//$Fe_2O_3$ nanoflakes AASCs exhibits a sharp peak (Fig. 5C) at approximately 1.5 V (corresponding to (0.35+1.15)V) during charging process under the potential window of 0~1.8 V. And the sharp peak at about 0.85 V during discharging is also in good accordance with the data of three-electrode systems. Besides, Fig. 5C also shows that increasing the potential limit from 1.0 to 1.8 V, more pseudocapacitance of $Fe_2O_3$ nanowires and NiO nanoflakes can be utilized with the enlarged area of CV curves. However, further increasing the potential to 1.9 V, the CV curve becomes distorted at the high potential arising from decomposition of water. Accordingly, the GCD curves in Fig. 5D also show that with increasing potential limit from 1.0 to 1.8 V, more pseudocapacitance of the full cell can utilized with longer charging-discharging platforms. And the corresponding specific capacitance increases from 48 to 240 $Fg^{-1}$ as well (Fig. S3). Besides, it was found that setting the potential limit to 1.9 V results in a platform approaching the upper limit due to the decomposition of water, which is also confirmed in CV curves. Furthermore, the coulombic efficiency under 0~1.8 V is as high as 91% (shown in Fig. S3), indicating the good reversible properties of the electrochemical process. Thus, 0~1.8 V is chosen as the safe potential window for the NiO nanoflakes//$Fe_2O_3$ nanowires AASCs, which is exactly the summation of the individual potential limit of anodes (1.35 V) and cathodes (0.45 V).

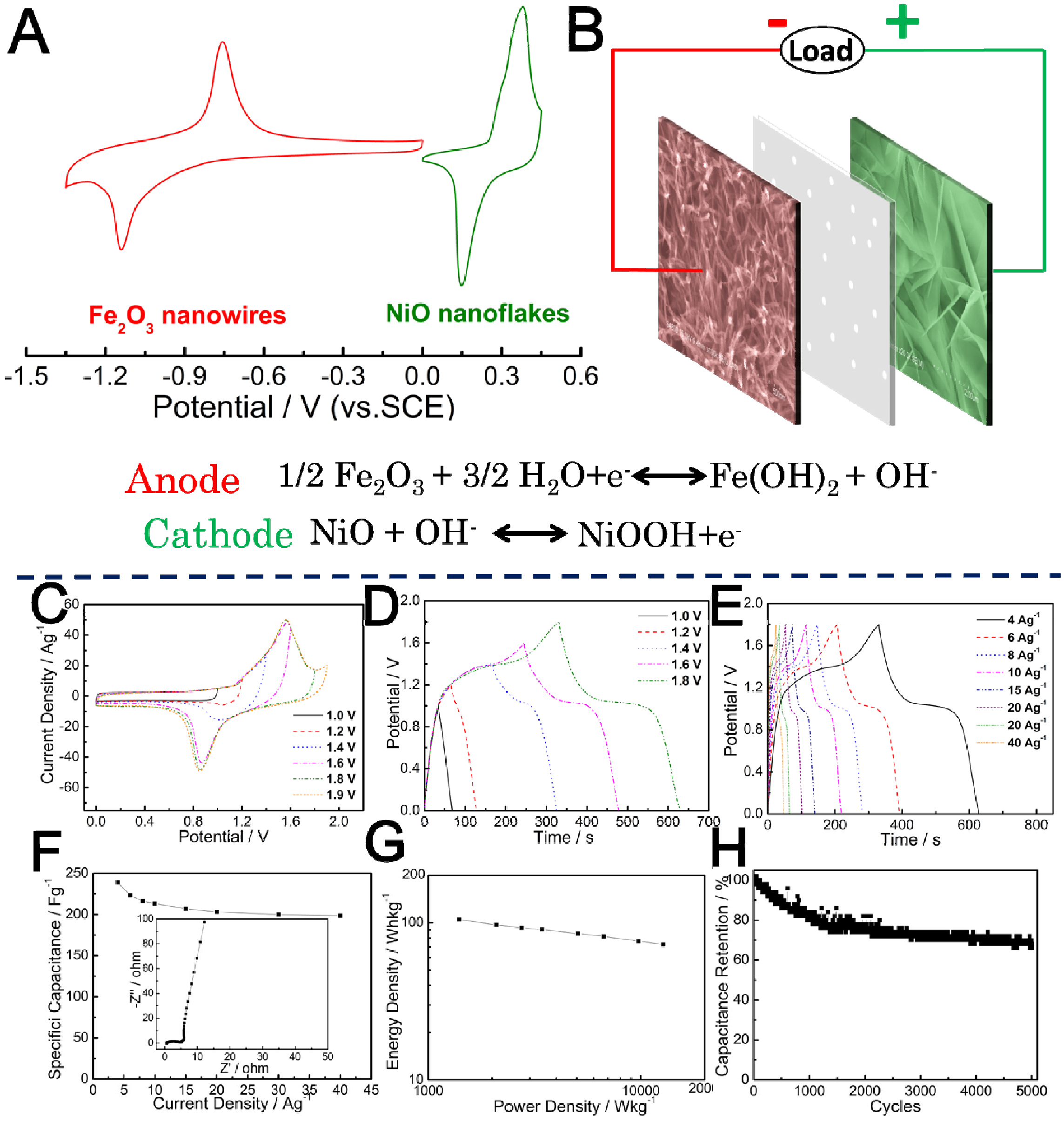

**Fig. 5**. (A) Cyclic voltammetry curves of NiO nanoflakes and $Fe_2O_3$ nanowires on CFP at 5 mV $s^{-1}$. (B) Schematic diagram of the as-assembled NiO nanoflakes//$Fe_2O_3$ nanowires AASCs. And electrochemical performance of the as-assembled NiO nanoflakes//$Fe_2O_3$ nanowires AASCs (C) cyclic voltammetry curves at various potential window at 5 mV $s^{-1}$. (D) Galvanostatic charge-discharge curves at the current density of 4 A $g^{-1}$ under various potential windows. (E) Galvanostatic charge-discharge curves at various current densities from 4 to 40 A $g^{-1}$ under the potential window of 0~1.8 V (based on the mass of $Fe_2O_3$ nanowires on CFP). (F) Specific capacitance at various current densities, which are based on the total mass of NiO nanoflakes and $Fe_2O_3$ nanowires on CFP (inserted with Nyquist plots in the frequency range of 100 kHz to 0.01 Hz). (G) Ragone plot. (H) Capacitance retention rate with cycle number at a current density of 5 A $g^{-1}$ (based on the mass of $Fe_2O_3$ nanowires on CFP) in the potential window of 0~1.8 V.

Furthermore, even at a high current density of 15 A $g^{-1}$, the GCD curve (Fig. 5E) still exhibits negligible IR drop at 1.8 V, showing the small internal resistance. It is also reflected from its Nyquist plot inserted in Fig. 5F by a small real axis intersection of 0.6 Ω. A small charge transfer resistance is confirmed by the small diameter of the semicircle of only 4.1 Ω. The nearly vertical line versus real axis shows their ideal capacitance properties. Calculated from GCD curves based on the total mass of $Fe_2O_3$ nanowires and NiO nanoflakes, the as-assembled AASC exhibits a high specific capacitance of 240 F $g^{-1}$ at 4 A $g^{-1}$ and still retains 199 F g$^{-1}$ at 40 A g$^{-1}$ (Fig. 5F). Furthermore, we provided the corresponding Ragone plot in Fig. 5G, an extremely high energy density of 105 Wh kg$^{-1}$ is obtained at the power density of 1400 W kg$^{-1}$ and retains 72.6 Wh kg$^{-1}$ at 12700 W kg$^{-1}$. Such an remarkable electrochemical performance is much superior to most of reported AASCs in literatures as shown in Table 1 especially with its significantly enhanced energy density.

As far as we know, there have been many literatures reporting pseudocapacitive cathodes with comparable good capacitive performance as ours or even better. Thus, the significantly enhanced electrochemical performance of our NiO nanoflakes//$Fe_2O_3$ nanowires AASCs compared with previous reported literatures is mainly attributed to the perfect $Fe_2O_3$ nanowires anode with broader negative potential window and larger specific pseudocapacitance. For example, NiMn-LDH/CNT cathode is reported to deliver a high specific capacitance (2960 F g$^{-1}$ at 1.5 A g$^{-1}$) with good rate capability, which is much higher than our NiO nanoflakes on CFP (1520 F g$^{-1}$ at 2A g$^{-1}$). However, when matching NiMn-LDH/CNT cathode with a reduced graphene oxide/carbon nanotube (RGO/CNT) film anode, a maximum energy density of only 88.3 Wh kg$^{-1}$ (at a power density of 850 W kg$^{-1}$) is obtained[51], which is lower than our NiO nanoflakes//$Fe_2O_3$ nanowires AASCs. This is due to the restriction of the relatively low specific capacitance of RGO/CNT anode, which adds much more total mass to the full AASCs so as to meet the charge balance between cathodes and anodes.

The cycling stability of the as-assembled AASCs is further evaluated by means of GCD cycling between 0~1.8 V at the current density of 5 A g$^{-1}$ shown in Fig. 5H. It shows an initial capacitance decrease of 20 % in the first 1000 cycles. After that, the capacitance decrease slows down. Up to the 5000th cycle, the capacitance retention rate is 68%. It shows an initial capacitance decrease of 20 % in the first 1000 cycles. After that, the capacitance decrease slows down. Up to the 5000th cycle, the capacitance retention rate is 68%. In order to study the causes for the capacitance reduction, FE-SEM images for $Fe_2O_3$ anode and NiO cathodes after 5000 cycles of GCD are provided in Fig. S4. As can be from Fig. S4A and S4B, the morphology of $Fe_2O_3$ nanowires have turned to small aggregated particles with a diameter of about 20 nm. And the NiO on CFP (Fig. S4C and S4D) shows no obvious morphology change and remains as homogeneous nanoflakes. Thus, the capacitance reduction of the assembled NiO nanoflakes//$Fe_2O_3$ nanowires AASCs may be mainly ascribed to the relatively poor stability of $Fe_2O_3$ anode caused by Fe dissolution in the electrolyte[20] and its structural change during charging and discharging process. Furthermore, Nyquist plots before and after 5000 cycles of GCD are also provided in Fig. S5. Larger charge-transfer resistance and more inclined curve to Z' axis in the low frequencies are observed after 5000 cycles, which is mainly due to the more aggregated structure of $Fe_2O_3$ anode and its irreversible redox reactions during charging-discharging. When compared with previous reports on iron-based electrodes or assembled-supercapacitors, the cycling stability of our NiO nanoflakes//$Fe_2O_3$ nanowires AASCs shows enhancement. For example, the graphene/$Fe_2O_3$ electrode[20] loses up to 25% initial capacitance at 20 mVs$^{-1}$ in the first 200 cycles and the $Fe_2O_3$/N-rGO loses 43.3% at 4 A g$^{-1}$ after 5000 cycles. Next, we are going to focus on improving the cycling stability of the $Fe_2O_3$-based AASCs, such as by coating $Fe_2O_3$ with conductive polymers.

**Table 1.** Performance for selected aqueous asymmetric supercapacitors.

| Cathode | Anode | Voltage window /V | E / Whkg$^{-1}$ | P / Wkg$^{-1}$ | Ref. |
|---|---|---|---|---|---|
| $Ni(OH)_2$-$MnO_2$-RGO | Reduced graphene oxide | 1.6 | 54.0 | 392 | 52 |
| $Ni(OH)_2$ | Porous activated carbon | 1.6 | ~68 ($E_{max}$) | 44000 ($P_{max}$) | 53 |
| Carbon-$MnO_2$ | Activated carbon | 2.0 | 63 | 227 | 25 |
| NiO | 3D graphene | 1.5 | ~42 | ~11000 | 28 |
| NiMn-LDH/CNT | reduced graphene oxide/carbon nanotubes | 1.7 | 88.3 | 850 | 51 |
| $NiCo_2O_4$/graphene | Highly functionalized activated carbon | 1.55 | 48 | 230 | 48 |
| $MnO_2$/GNS | FeOOH/GNS/CNTs | 1.7 | 30.4 | 237.6 | 26 |
| HCoOx@$Ni(OH)_2$ core–shell NWs | fRGO@$Fe_3O_4$ | 1.7 | 45.3 | 1010 | 54 |
| CFP@ $NiCo_2O_4$ | Graphene foam | 1.6 | 34.5 | 547 | 24 |

## 4. Conclusions

In summary, a novel low-cost anode of homogenous $Fe_2O_3$ nanowires growing on CFP is prepared through a simple process. Taking advantages of the nanostructures of $Fe_2O_3$ nanowires with a small diameter of about 10 nm, they exhibits a high specific capacitance of 908 F g$^{-1}$ at 2A g$^{-1}$ and excellent rate performance (90 % capacitance retention up to 10 A g$^{-1}$) in a wide potential window of 0~-1.35 V. Cathode of NiO nanoflakes prepared through a similar process exhibits an excellent capacitive behavior of 1520 F g$^{-1}$ at 2 A g$^{-1}$ in 0~0.45 V. The complementary potential window and excellent capacitive behavior make the as-prepared $Fe_2O_3$ nanowires a perfect candidate to match with NiO nanoflakes cathode, achieving a high total specific capacitance of 240 F g$^{-1}$ for the assembled AASCs in the potential window of 1.8 V. Furthermore, an extremely high energy density of 105 Wh kg$^{-1}$ is obtained at the power density of 1400 W kg$^{-1}$ and still retains 72.6 Wh kg$^{-1}$ at 12700 Wkg$^{-1}$, which is much superior to most of reported AASCs and exceeding those of Ni-MH batteries. Thus, the low-cost $Fe_2O_3$ nanowires anode with such a remarkable supercapacitive performance holds great promise for application in high-energy-density supercapacitors in the real world.

## Acknowledgements

This work was supported by National Natural Science Foundation of China (51173042), Shanghai Municipal Science and Technology Commission (12nm0504102), and Fundamental Research Funds for the Central Universities.

## Notes and references

[a] *Shanghai Key Laboratory of Advanced Polymeric Materials, Key Laboratory for Ultrafine Materials of Ministry of Education, School of Materials Science and Engineering, East China University of Science and Technology, Shanghai 200237, P.R.China. E-mail: gengchaow@ecust.edu.cn*

† Electronic Supplementary Information (ESI) available: Experimental details and supplementary figures. See DOI: 10.1039/b000000x/

1 J. Yan, Z. Fan, W. Sun, G. Ning, T. Wei, Q. Zhang, R. Zhang, L. Zhi and F. Wei, *Adv. Funct. Mater.* 2012, **22**, 2632-2641.
2 Z. Fan, J. Yan, T. Wei, L. Zhi, G. Ning, T. Li and F. Wei, *Adv. Funct. Mater.* 2011, **21**, 2366-2375.
3 V. Khomenko, E. Raymundo-Pinero and F. Beguin, *J. Power Sources* 2006, **153**, 183-190.
4 J. Jiang, Y. Y. Li, J. P. Liu, X. T. Huang, C. Z. Yuan and X. W. Lou, *Adv. Mater.* 2012, **24**, 5166-5180.
5 Z. B. Lei, F. H. Shi and L. Lu, *ACS Appl. Mater. Interfaces* 2012, **4**, 1058-1064.
6 Y. Z. Su, K. Xiao, N. Li, Z. Q. Liu and S. Z. Qiao, *J. Mater. Chem. A* 2014, **2**, 13845-13853.
7 H. Chen, L. F. Hu, M. Chen, Y. Yan and L. M. Wu, *Adv. Funct. Mater.* 2014, **24**, 934-942.
8 J. Duay, S. A. Sherrill, Z. Gui, E. Gillette and S. B. Lee, *ACS Nano* 2013, **7**, 1200-1214.
9 M. Salari, K. Konstantinov and H. K. Liu, *J. Mater. Chem.* 2011, **21**, 5128-5133.
10 C. Y. Cao, W. Guo, Z. M. Cui, W. G. Song and W. Cai, *J. Mater. Chem.* 2011, **21**, 3204-3209.
11 F. L. Zheng, G. R. Li, Y. N. Ou, Z. L. Wang, C. Y. Su and Y. X. Tong, *Chem. Commun.* 2010, **46**, 5021-5023.
12 J. Xu, K. Wang, S. Z. Zu, B. H. Han and Z. Wei, *ACS Nano* 2010, **4**, 5019-5026.
13 G. Wee, H. Z. Soh, Y. L. Cheah, S. G. Mhaisalkar and M. Srinivasan, *J. Mater. Chem.* 2010, **20**, 6720-6725.
14 H. Wang, Q. Hao, X. Yang, L. Lu and X. Wang, *Nanoscale* 2010, **2**, 2164-2170.
15 W. Chen, Z. Fan, L. Gu, X. Bao and C. Wang, *Chem. Commun.* 2010, **46**, 3905-3907.
16 Q. T. Qu, Y. Shi, L. L. Li, W. L. Guo, Y. P. Wu, H. P. Zhang, S. Y. Guan and R. Holze, *Electrochem. Commun.* 2009, **11**, 1325-1328.
17 Z. Chen, Y. Qin, D. Weng, Q. Xiao, Y. Peng, X. Wang, H. Li, F. Wei and Y. Lu, *Adv. Funct. Mater.* 2009, **19**, 3420-3426.
18 D. Choi, G. E. Blomgren and P. N. Kumta, *Adv. Mater.* 2006, **18**, 1178-1182.
19 Y. C. Chen, Y. G. Lin, Y. K. Hsu, S. C. Yen, K. H. Chen and L. C. Chen, *Small* 2014, **10**, 3803-3810.
20 H. Wang, Z. Xu, H. Yi, H. Wei, Z. Guo and X. Wang, *Nano Energy* 2014, **7**, 86-96.
21 W. J. Meng, W. Chen, L. Zhao, Y. Huang, M. S. Zhu, Y. Q. Fu, F. X. Geng, J. Yu, X. F. Chen and C. Y. Zhi, *Nano Energy* 2014, **8**, 133-140.
22 B. H. Zhang, Y. Liu, Z. Chang, Y. Q. Yang, Z. B. Wen, Y. P. Wu and R. Holze, *J. Power Sources* 2014, **253**, 98-103.
23 S. J. Zhu, W. L. Cen, L. L. Hao, J. J. Ma, L. Yu, H. L. Zheng and Y. X. Zhang, *Mater. Lett.* 2014, **135**, 11-14.
24 Q. Tang, M. M. Chen, L. Wang and G. Wang, *J. Power Sources* 2015, 654-662.
25 C. L. Long, D. P. Qi, T. Wei, J. Yan, L. L. Jiang and Z. J. Fan, *Adv. Funct. Mater.* 2014, **24**, 3953-3961.
26 C. L. Long, L. L. Jiang, T. Wei, J. Yan and Z. J. Fan, *J. Mater. Chem. A* 2014, **2**, 16678-16686.
27 R. T. Wang, X. B. Yan, J. W. Lang, Z. M. Zheng and P. Zhang, *J. Mater. Chem. A* 2014, **2**, 12724-12732.
28 C. D. Wang, J. L. Xu, M. F. Yuen, J. Zhang, Y. Y. Li, X. F. Chen and W. J. Zhang, *Adv. Funct. Mater.* 2014, **24**, 6372-6380.
29 Y. Yoon, K. Lee, S. Kwon, S. Seo, H. Yoo, S. Kim, Y. Shin, Y. Park, D. Kim, J. Y. Choi and H. Lee, *ACS Nano* 2014, **8**, 4580-4590.
30 H. P. Cong, X. C. Ren, P. Wang and S. H. Yu, *Energy Environ. Sci.* 2013, **6**, 1185-1191.
31 X.-C. Dong, H. Xu, X.-W. Wang, Y.-X. Huang, M. B. Chan-Park, H. Zhang, L.-H. Wang, W. Huang and P. Chen, *ACS Nano* 2012, **6**, 3206-3213.
32 L. Bao, J. Zang and X. Li, *Nano Lett.* 2011, **11**, 1215-1220.
33 W. Tang, L. Liu, S. Tian, L. Li, Y. Yue, Y. Wu and K. Zhu, *Chem. Commun.* 2011, **47**, 10058-10060.
34 Z. L. Ma, X. B. Huang, S. Dou, J. H. Wu and S. Y. Wang, *J. Phys. Chem. C* 2014, **118**, 17231-17239.
35 P. Yang, Y. Ding, Z. Lin, Z. Chen, Y. Li, P. Qiang, M. Ebrahimi, W. Mai, C. P. Wong and Z. L. Wang, *Nano Lett.* 2014, **14**, 731-736.
36 L. F. Chen, Z. Y. Yu, X. Ma, Z. Y. Li and S. H. Yu, *Nano Energy* 2014, **9**, 345-354.
37 Q. Qu, S. Yang and X. Feng, *Adv. Mater.* 2011, **23**, 5574-5580.
38 Q. Qu, Y. Zhu, X. Gao and Y. Wu, *Adv. Energy Mater.* 2012, **2**, 950-955.
39 W. Tang, L. Liu, Y. Zhu, H. Sun, Y. Wu and K. Zhu, *Energy Environ. Sci.* 2012, **5**, 6909-6913.
40 J. Hu, A. Ramadan, F. Luo, B. Qi, X. Deng and J. Chen, *J. Mater. Chem.* 2011, **21**, 15009-15014.
41 G. Q. Zhang, H. B. Wu, H. E. Hoster, M. B. Chan-Park and X. W. Lou, *Energy Environ. Sci.* 2012, **5**, 9453-9456.
42 H. Wu, M. Xu, H. Y. Wu, J. J. Xu, Y. L. Wang, Z. Peng and G. F. Zheng, *J. Mater. Chem.* 2012, **22**, 19821-19825.
43 Y. Q. Song, S. S. Qin, Y. W. Zhang, W. Q. Gao and J. P. Liu, *J. Phys. Chem. C* 2010, **114**, 21158-21164.
44 L. Vayssieres, N. Beermann, S. E. Lindquist and A. Hagfeldt, *Chem. Mater.* 2001, **13**, 233-235.
45 T. Yamashita and P. Hayes, *Appl. Surf. Sci.* 2008, **254**, 2441-2449.
46 X. Lu, Y. Zeng, M. Yu, T. Zhai, C. Liang, S. Xie, M.-S. Balogun and Y. Tong, *Adv. Mater.* 2014, **26**, 3148-3155.
47 E. McCafferty and J. P. Wightman, *Surf. Interface Anal.* 1998, **26**, 549-564.
48 Z. Li, Z. W. Xu, H. L. Wang, J. Ding, B. Zahiri, C. M. B. Holt, X. H. Tan and D. Mitlin, *Energy Environ. Sci.* 2014, **7**, 1708-1718.
49 J. W. Xiao and S. H. Yang, *J. Mater. Chem.* 2012, **22**, 12253-12262.
50 M. W. Nydegger, G. Couderc and M. A. Langell, *Appl. Surf. Sci.* 1999, **147**, 58-66.
51 J. W. Zhao, J. Chen, S. M. Xu, M. F. Shao, Q. Zhang, F. Wei, J. Ma, M. Wei, D. G. Evans and X. Duan, *Adv. Funct. Mater.* 2014, **24**, 2938-2946.
52 H. Chen, S. X. Zhou and L. M. Wu, *ACS Appl. Mater. Interfaces* 2014, **6**, 8621-8630.
53 Y. Yang, L. Li, G. D. Ruan, H. L. Fei, C. S. Xiang, X. J. Fan and J. M. Tour, *ACS Nano* 2014, **8**, 9622-9628.
54 J. X. Zhu, L. Huang, Y. X. Xiao, L. Shen, Q. Chen and W. Z. Shi, *Nanoscale* 2014, **6**, 6772-6781.